Finite-Element Analysis for Photoelastic Tactile Sensors

R. E. Saad
Department of Electrical & Computer Engineering

A. Bonen
Department of Electrical & Computer Engineering

K. C. Smith
Department of Electrical & Computer Engineering

B. Benhabib*
Department of Mechanical Engineering

Computer Integrated Manufacturing Laboratory, University of Toronto
5 King's College Road, Toronto, Ontario, Canada M5S 1A4
*e-mail: beno@me.utoronto.ca

Abstract — **In this paper, a photoelastic tactile transducer is modelled and analyzed using Finite-Element Analysis (FEA). The effects of both normal and tangential forces are considered. Two different boundary conditions are examined for a transducer whose compliant protective layer has different mechanical properties from the photoelastic layer.**

I. INTRODUCTION

Photoelasticity, in the context of tactile sensing, is an optical phenomenon that has not received wide attention in the literature [1-6]. The few studies that have been published on photoelastic tactile sensors include the description [4] and implementation of a basic sensor [5], as well as a theoretical model used to analyze it [6]. Research results presented in these papers clearly show that a photoelastic transducer can satisfy many of the tactile-sensing requirements specified by Harmon [7].

Photoelastic sensors have also been developed to detect slippage. One such sensor [8] uses a transducer similar to the one described in [4,5]. However, in [8], direct analysis of the fringes is used to detect movement of the grasped object [9].

The photoelastic tactile transducer considered in this paper was developed in our laboratory as detailed earlier in [2,3]. Thus, only a brief explanation of it is provided herein. The transducer consists of a fully-supported two-layer beam, with a mirrored surface between the two layers, Fig. 1. The second, compliant, layer is added to protect the rear surface of the mirror. In our analysis, it is assumed that line-distributed forces, separated by an equal distance (s) from each other, are applied to a section of the top surface of the beam. A general angle α_j defines the direction of the (j^{th}) applied line force, F_j, with respect to the surface normal. The applied force at the j^{th} position (tactel), thus, has both normal, N_j , and tangential, T_j, components.

The illumination of a photoelastic transducer is typically achieved using a polaridoscope [10]. The output light-intensity distribution from the polaridoscope is created by the birefringence induced in the photoelastic layer by forces applied onto the transducer. The birefringence creates a phase-lead distribution that modulates the output light intensity [11].

The phase-lead distribution, as will be shown in Section II, is related to the stress distribution by the photoelasticity law. Because of the complexity of the structure of the transducer, the stress distribution must be calculated using Finite-Element Analysis (FEA). This analysis must account for boundary conditions (BCs) applied to the transducer which influence the stress distribution, and consequently, the phase-lead distribution.

II. MODEL OF THE TRANSDUCER

When forces are applied onto a photoelastic transducer, stresses are induced in it. The analytical calculation of the stresses is nearly impossible due to the complexity of BCs associated with the transducer and the different mechanical properties of the compliant protective and photoelastic transducer layers.

FEA has been widely used in the literature to estimate stresses for such complex problems. In the particular case of tactile sensing, FEA has been utilized in several recent works aimed at developing improved models for the increasingly complex transducer designs [12-16].

The first step in FEA is the definition of an appropriate mesh for the object (transducer) under stress. The number of elements used in the mesh directly affects the accuracy of the results. However, the number of elements may be restricted by the limitation of the FEA software (ANSYS in our case).

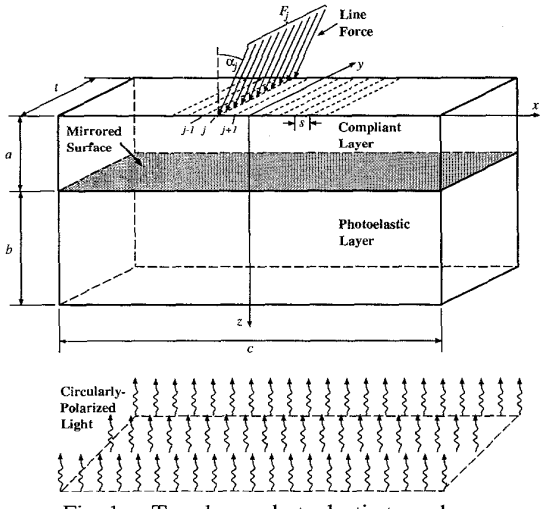

Fig. 1. Two-layer photoelastic transducer.

For the transducer considered in this paper, a large number of nodes is necessary along the x-axis. Thus, a compromise in choosing the node distribution must be reached for modeling the transducer. Because of the symmetry of the forces applied to the transducer along the y-axis, it is assumed that the stress distribution is constant along the y-axis, and a 2-D analysis is used in the x-z plane of the transducer. Plane-stress BCs are assumed for the FEA [17]. For the example presented in this paper, the number of elements used in the mesh was 5,025. The number of nodes along the x-axis, M, and the z-axis, L are 201 and 25, respectively. Fig. 2 shows the 2-D mesh configuration selected for the analysis. The central part of the mesh has more elements than the outer parts in order to improve the accuracy of the stress calculations in the central region where the forces are applied. E_1 and ν_1, and E_2 and ν_2 denote the modulii of elasticity and Poison's coefficients of the compliant and the photoelastic layers, respectively.

The values of the stresses are directly related to the BCs of the transducer. Two different BCs were considered: The first one, shown in Fig. 3 (a), assumes that only the bottom part of the transducer is fully supported and the lateral borders are free (*Case 1*). The second one, shown in Fig. 3 (b), assumes that the bottom part of the transducer is fully supported and that the lateral borders can move only in the vertical direction (*Case 2*). These BCs represent two possible practical cases in the design of a photoelastic transducer, and, as will be discussed in Section IV, influence the dynamic range of the sensor.

The calculation of the induced phase-lead distribution can be carried out using the photoelasticity law that links the stress distribution to the phase-lead distribution [10]. In our case, the phase-lead distribution $p(x)$ can be calculated following [6] as:

$$p(x)=2K_t\int_a^{a+b}\sigma_x(x,z)dz\,, \tag{1}$$

where K_t is a constant and σ_x is the shear stress along the x-axis, when a set of arbitrary forces (N_j and T_j) is applied. The constant K_t is given by:

$$K_t=\frac{1+\nu_2}{E_2}K_s\frac{2\pi}{\lambda}\,, \tag{2}$$

where λ is the wavelength of the light and K_s is the photoelastic strain coefficient.

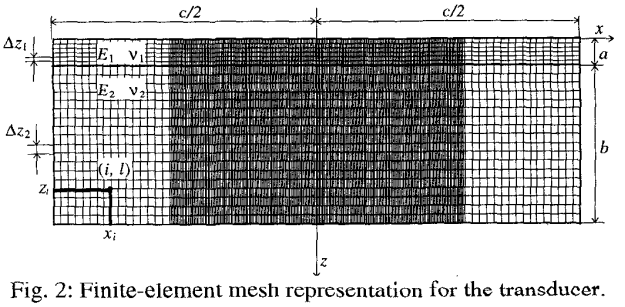

Fig. 2: Finite-element mesh representation for the transducer.

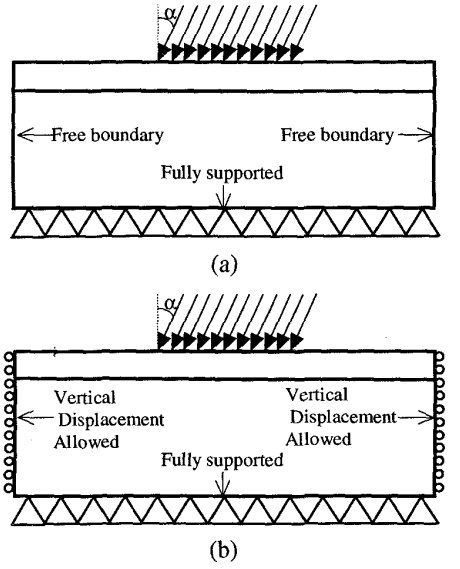

Fig. 3. Boundary conditions.

Since the stresses are calculated at each node of the mesh by FEA, (1) is re-written as:

$$p_i=2K\sum_{l=1}^{L}\sigma_{il}\Delta z_2\,, \tag{3}$$

where p_i is the phase-lead at x_i, σ_{il} is the shear stress at the node (i,l), and Δz_2 is the distance between two consecutive nodes along the z-axis in the photoelastic layer.

The specific parameters and dimensions of the transducer given in Tables I and II were used in the numerical examples below. N_t denotes the total number of tactels at which line forces are applied.

Case 1. For this case, the resulting stress profiles at three different depths are shown in Fig. 4 for a set of forces of 1 N applied at an angle α=10° at each tactel. Due to the particular BC, the stress values at the borders of the transducer must be zero. As can be observed in Fig. 4, the photoelastic layer acts as low-pass filter: The stress distribution is smoothed as the depth of the photoelastic layer increases [12].

Case 2. In Fig. 5, the stress profiles are shown for the same set of forces and at the same depths used in Case 1. Here, however, due to the specific BC, the stress values at the borders do not necessarily have to be zero.

TABLE I.
DIMENSIONS OF THE TRANSDUCER

a	b	c	s	t
0.5 mm	3 mm	25 mm	1 mm	2 mm

TABLE II.
OPTO-MECHANICAL PROPERTIES OF THE TRANSDUCER

E_1	E_2	ν_1	ν_2	λ	K_s	N_t
11 MPa	110 MPa	0.49	0.42	632.8 nm	0.05	11

The corresponding phase-lead distributions for Cases 1 and 2 can be calculated using (3). As can be observed from Fig. 6, the value of the phase-lead at x=0, is zero for Case 1[1] and non-zero for Case 2. Thus, one can conclude that the BCs of the transducer directly affect the BCs of the phase-lead distribution. On the other hand, it is also interesting to note that for the example under analysis, the BCs do not affect the phase-lead distribution at some distance from the boundary. A potential reason for this phenomenon is that, for our example, the transducer is long enough to reduce the effect of the BCs in the central part. Presumably, if the transducer had been shortened, the BCs would affect the phase-lead distribution along its full length.

III. GENERAL CHARACTERIZATION OF THE TRANSDUCER

Running the FEA program every time that a new force profile is applied to the transducer would be extremely time-consuming. Since the opto-mechanical system is seen to be linear, the principle of superposition applies. (In fact, this is what underlies the FEA technique used.)

Applying the principle of superposition more globally, the stresses σ_{il} can be seen as the individual contributions of the stresses generated by the sets of normal and shear forces applied to the transducer. Equation (3) can be then re-written as:

$$p_i = 2K\sum_{l=1}^{L} {}^{N}\sigma_{il}\Delta z_2 + 2K\sum_{l=1}^{L} {}^{T}\sigma_{il}\Delta z_2 , \qquad (4)$$

where ${}^{N}\sigma_{il}$ and ${}^{T}\sigma_{il}$ are, respectively, the stresses due to the normal and tangential forces applied to the transducer.

Since the system is linear with multiple inputs, the stresses ${}^{N}\sigma_{il}$ and ${}^{T}\sigma_{il}$ can be considered as the superposition of the individual stresses generated by each of the normal and tangential components of the input forces. Those individual stresses are denoted ${}^{N}_{j}\sigma_{il}$ and ${}^{T}_{j}\sigma_{il}$, where j identifies the tactel that is producing them. Based on that, (4) can be re-written as:

$$p_i = 2K\sum_{l=1}^{L}\sum_{j=1}^{N_t} {}^{N}_{j}\sigma_{il}\Delta z_2 + 2K\sum_{l=1}^{L}\sum_{j=1}^{N_t} {}^{T}_{j}\sigma_{il}\Delta z_2 \qquad (5)$$

The individual impulse response of each tactel can be found by applying known normal (W_N) and tangential (W_T) loads at each tactel and calculating the corresponding shear stresses at each node. Let those stresses be denoted as ${}^{N}_{j}\sigma^{*}_{il}$ and ${}^{T}_{j}\sigma^{*}_{il}$. Equation (5) can be then re-written as:

$$p_i = 2K\sum_{l=1}^{L}\sum_{j=1}^{N_t} \frac{1}{W_N} {}^{N}_{j}\sigma^{*}_{il} N_j \Delta z_2 + 2K\sum_{l=1}^{L}\sum_{j=1}^{N_t} \frac{1}{W_T} {}^{T}_{j}\sigma^{*}_{il} T_j \Delta z_2 . \qquad (6)$$

Re-arranging (6) results in:

[1] From Fig. 6, it can be observed that, in reality, the phase-lead distribution for Case 1 at x=0 is not exactly zero due to small numerical errors in the stress calculation.

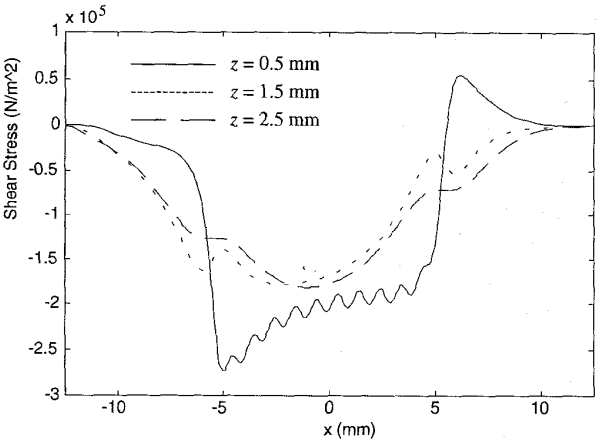

Fig. 4. Shear-stress distribution at depths of 0.5, 1.5 and 2.5 mm for Case 1.

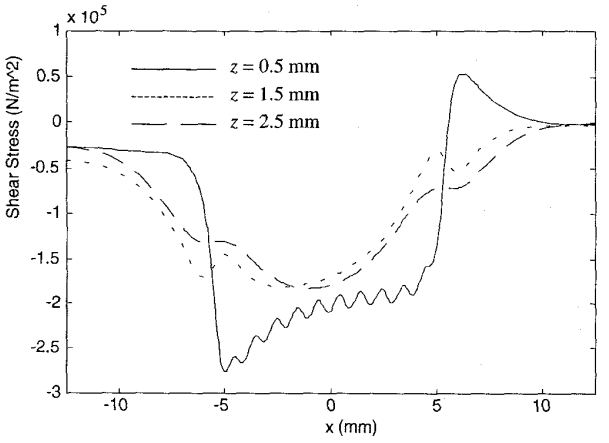

Fig. 5. Shear stress distribution at depths of 0.5, 1.5 and 2.5 mm for Case 2.

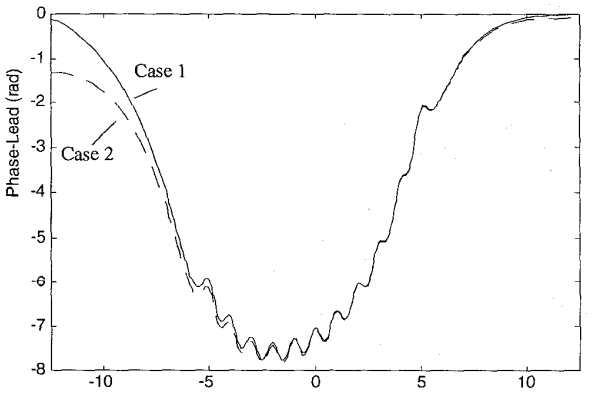

Fig. 6. Phase-lead distribution when a load of 1 N is applied to each of the 11 tactels at angle of 10°.

$$p_i = \frac{1}{W_N}\sum_{j=1}^{N_t} N_j \left(2K \sum_{l=1}^{L} {}^{N}_{j}\sigma^{*}_{il}\Delta z_2 \right) + \frac{1}{W_T}\sum_{j=1}^{N_t} T_j \left(2K \sum_{l=1}^{L} {}^{T}_{j}\sigma^{*}_{il}\Delta z_2 \right) . \quad (7)$$

The expressions in parentheses indicate the corresponding phase leads at the x_i coordinate with respect to the known loads W_N and W_T applied to the j^{th} tactel. Such phase leads can be notated as ${}^{N}\psi_{ij}$ and ${}^{T}\psi_{ij}$, respectively. Then, (7) is reduced to:

$$p_i = \frac{1}{W_N}\sum_{j=1}^{N_t} {}^{N}\psi_{ij} N_j + \frac{1}{W_T}\sum_{j=1}^{N_t} {}^{T}\psi_{ij} T_j . \quad (8)$$

The equivalent matrix form of (8) is given by:

$$\mathrm{P} = \frac{1}{W_N}\Psi_N \mathrm{N} + \frac{1}{W_T}\Psi_T \mathrm{T} , \quad (9.a)$$

where

$$\mathrm{P} = \begin{bmatrix} p_1 \\ \vdots \\ p_M \end{bmatrix}, \ \mathrm{N} = \begin{bmatrix} N_1 \\ \vdots \\ N_{N_t} \end{bmatrix}, \mathrm{T} = \begin{bmatrix} T_1 \\ \vdots \\ T_{N_t} \end{bmatrix} , \quad (9.b)$$

and

$$\Psi_N = \begin{bmatrix} {}^{N}\psi_{11} \cdots {}^{N}\psi_{1N_t} \\ \vdots \quad\quad \vdots \\ {}^{N}\psi_{M1} \cdots {}^{N}\psi_{MN_t} \end{bmatrix} \quad \Psi_T = \begin{bmatrix} {}^{T}\psi_{11} \cdots {}^{T}\psi_{1N_t} \\ \vdots \quad\quad \vdots \\ {}^{T}\psi_{M1} \cdots {}^{T}\psi_{MN_t} \end{bmatrix} . \quad (9.c)$$

Fig. 7, shows the phase-lead distributions ${}^{N}\psi_{i1}$ and ${}^{T}\psi_{i1}$ for $i=1,2,\ldots M$ considering that W_N=0.4 N and W_T=0.2 N.

Assuming $W_N=W_T=W$, (8) can be re-written as:

$$\mathrm{P} = \frac{1}{W}\Psi \mathrm{F} , \quad (10.a)$$

where,

$$\Psi = \left[\Psi_N \vdots \Psi_T \right] \quad \mathrm{F} = \begin{bmatrix} \mathrm{N} \\ \cdots \\ \mathrm{T} \end{bmatrix} . \quad (10.b)$$

Equation (10) completely characterizes the transducer. The model matrix Ψ takes into account the parameters and dimensions of the transducer, as well as, the BCs. Once it is evaluated, FEA programs are no longer needed for the forward analysis of that particular transducer. Equation (10) also provides the means for solving the inverse-problem of the tactile sensor: If P and Ψ are known, F, can be calculated by inverting (10.a).

IV. INFLUENCE OF THE BOUNDARY CONDITIONS ON THE DYNAMIC RANGE

When a polaridoscope is used to illuminate the transducer, the phase-lead distribution cannot be measured directly [10]. Instead, the light-intensity distribution is measured. For the ideal (noise-free) case, the normalized light-intensity distribution is a function of the phase-lead distribution [10]:

$$I(x) = \sin^2 \frac{p(x)}{2} \quad (11)$$

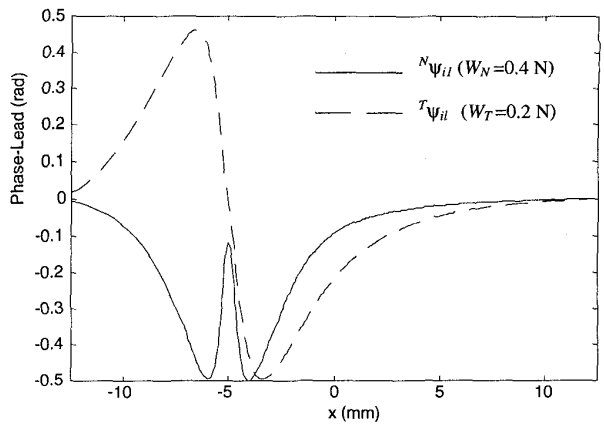

Fig. 7. Phase-lead distribution ${}^{N}\psi_{il}$ and ${}^{T}\psi_{i}$, i=1,2...M when W_N=0.4 N and W_T=0.2 N and the transducer is under the BCs specified for Case 1.

Recovering the phase-lead distribution from (11), requires the use of an algorithm previously reported, since the phase-lead distribution might not be limited to the interval [-π 0] over the length of the transducer [1]. Fig. 6 is an example of this possible case. Fig. 8 shows the corresponding normalized light-intensity distribution of the phase-lead distribution of Case 1.

The following algorithm is an analytical method for the recovery of a general phase-lead distribution from the normalized light-intensity distribution under ideal conditions. A detailed explanation of this algorithm has been previously reported in [1]

The first step in the algorithm is the classification of the critical points[2] of $I(x)$ as follows:

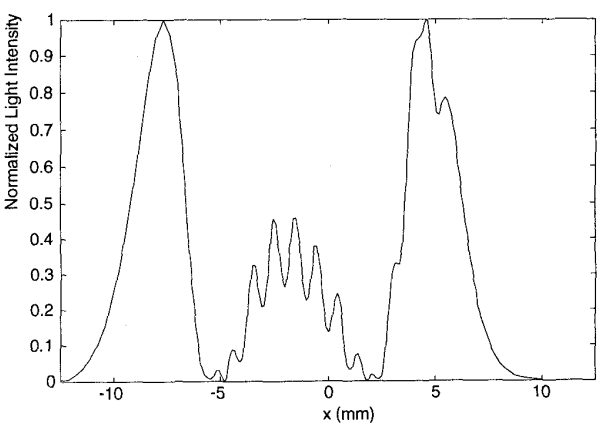

Fig. 8. Normalized light-intensity distribution for Case 1.

[2] Critical points of $I(x)$ are the those points where dI/dx=0.

(a) *Class 1*: critical points of $I(x)$, where $I(x)$=1, and the first non-negative derivative is of the form $d^{2k+1}I/dx^{2k+1}$ for some integer $k \geq 1$.

(b) *Class 2*: critical points of $I(x)$, where $I(x)$=0, and the first non-negative derivative is of the form $d^{2k+1}I/dx^{2k+1}$ for some integer $k \geq 1$.

(c) *Class 3:* critical points of $I(x)$, which are local extrema but do not satisfy conditions (a) or (b).

The second step in the algorithm deals with the recovery of the phase-lead distribution. The phase-lead distribution can be reconstructed using the following formula:

$$p(x) = -2\pi m - (-1)^{m+n} 2\arcsin\sqrt{I(x)} \quad , \qquad (12)$$

where $m \rightarrow m+(-1)^k$.

The algorithm starts with m=0, n=0, and k=0. The phase-lead distribution is recovered point-by-point by increasing x from $-l/2$ to $l/2$ (or vice versa). When a *Class 3* critical point is encountered, k is increased by one; when a *Class 2* critical point is encountered, n is increased by one; and, when a *Class 1* critical point is encountered, m is increased or decreased by one depending on the value of k.

Equation (12) assumes that the phase-lead distribution at the borders ($x=-l/2$ or $x=l/2$) is in the interval $U=[-\pi\ 0]$. This condition is a consequence of the initial values of m, n, and k. If the value of the phase-lead at the borders is not in the interval U, a new set of initial indices must be provided. Unfortunately, the initial values of the indices cannot be provided if the phase-lead distribution is not known a priori. For this reason it is imperative to guarantee that the value of the phase-lead at the borders is restricted to the interval U.

If the transducer has the BCs of Case 1, the above condition is guaranteed since the phase-lead values are zero at $x=-l/2$ and $x=l/2$, independently of the force applied to the transducer. But, if the transducer has the BCs of Case 2, the above condition is not guaranteed for the complete range of applied forces. Thus, the BCs for Case 1, provide a transducer with a larger dynamic range. It should be noted that this particular characteristic is not shared by other technologies (resistive, capacitive, for example), where the BCs do not substantially influence the dynamic range of the sensor.

V. INVERSE PROBLEM

In Sections II and III, forward analysis of the sensor was presented. In Section IV, an algorithm was presented for the solution of the inverse problem under ideal (noise-free) conditions. In reality, however, the light-intensity distribution is subject to noise from electronic sources, A/D conversion, and spatial sampling when a digital line-scan camera is used in the detection process. In this case, the light-intensity distribution is given by:

$$I_d(x_i) = round\left[A\sin^2\frac{p(x_i)}{2} + n_o(x_i) + I_o \right] \qquad (13)$$

where n_o is the total random noise introduced into the measurement; I_o is the minimum average normalized voltage applied to the A/D converter, such that $I_o + \min(n_o) \geq 0$; and A is the maximum allowed dynamic range of the A/D converter, such that $A + I_o + \max(n_o) \leq 2^B - 1$, where B is the number of bits in the A/D converter. The function $round(\cdot)$ returns the closest integer to the real number $(\cdot)$ and simulates the effect of the A/D converter.

Recovering the phase-lead distribution from (13) constitutes an ill-posed problem, since several phase-lead distribution can be recovered [3]. This occurs because the classification of the critical points of the light-intensity distribution becomes ambiguous. The added noise in the light-intensity distribution prevents the accurate calculation of high-order derivatives; thus, the critical points cannot be classified using the algorithm outlined in Section IV because of the noise conditions.

In [2,3], an algorithm that solves the noise-induced ill-posed inverse problem was reported. The algorithm accurately reconstructs the phase-lead distribution, and also recovers the applied force profile. Here, we limit our discussion to applying that algorithm to the example of Case 1.

In Fig. 9, the corresponding "noisy" light-intensity distribution for Case 1 is shown for the case in which B=8 bits, I_o=5, A=245, and that a linear array with 2,048 elements is used as a detector for measuring the light-intensity distribution. The noise n_o is assumed to be random and limited between -5 and 5 grey levels.

Using the algorithm in [3], the phase-lead distribution, P_r, shown in Fig. 10, is reconstructed. As can be observed this phase-lead distribution is slightly different from the original phase-lead distribution shown in Fig. 6 and reproduced in Fig. 10 for comparison purposes. Once the phase-lead distribution is recovered, the force profile can be obtained by solving the following equation for F_r [3]:

$$P_r = \frac{1}{W}\hat{\Psi}F_r \, , \qquad (14)$$

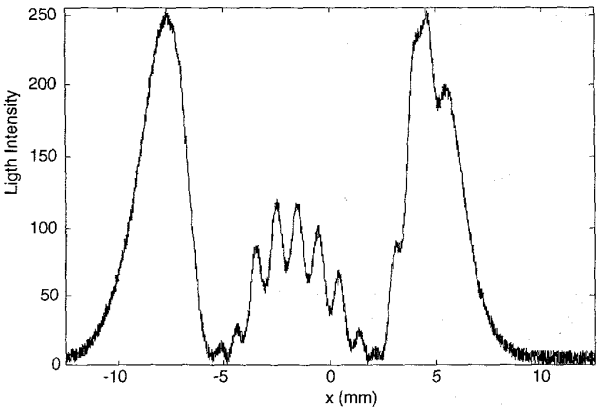

Fig 9. Noisy light-intensity distribution in grey levels.

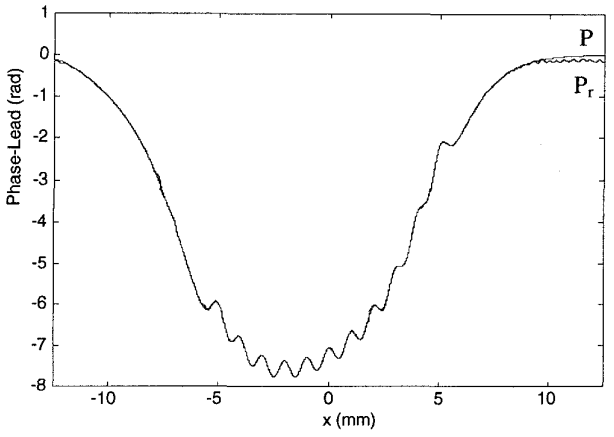

Fig. 10. Phase-lead distributions P and P_r for Case 1.

where $\hat{\Psi}$ is the model matrix obtained under noisy conditions [3] and F_r is the recovered force profile. F_r is obtained from (14) using a least-squares technique. The recovered force profile for our example is then given by:

$$F_r = (\ 0.976\angle 10.6^o,\ 1.02\angle 9.7^o,\ 1.05\angle 9.8^o,\ 0.97\angle 10.4^o,$$
$$0.963\angle 9.5^o,\ 0.98\angle 10.5^o,\ 0.973\angle 10.4^o,\ 0.967\angle 10.3^o,$$
$$0.953\angle 10.2^o,\ 0.943\angle 10.7^o,\ 1.056\angle 9.7^o)$$

When one compares this result with the actual applied force profile, one sees that the maximum error is less than 6% in the force magnitude and 7% in the angle of application for a noise of ±5 grey levels in the light-intensity distribution.

VI. CONCLUSIONS

In this paper, the forward analysis of a photoelastic tactile sensor is presented. The transducer of the sensor is modelled using FEA with a 2-D mesh representation. Two boundary conditions were considered. It was shown that the dynamic range of the sensor is directly influenced by the BCs applied. Also, it was shown that the transducer can be completely characterized by a phase-lead matrix Ψ. Finally, an algorithm, previously reported in [2,3], was successfully applied to solve the inverse problem under noisy conditions, simulating the actual measurement situation.

VII. ACKNOWLEDGMENT

The authors are grateful for the financial support provided by the Natural Sciences and Engineering Research Council of Canada. Mr. Saad would also like to thank CNPq, Brazil, for its financial support. Further, the authors would like to thank Dr. Tom Zougas for the development of the FEA programs.

VIII. REFERENCES

[1] R. E. Saad, B. Benhabib and K. C. Smith, "A Novel Photoelastic Tactile Transducer for Robotics", SME, Fifth World Conference on Robotics Research, Cambridge, Massachusetts, 1994, pp. 4-1:4-14.

[2] R. E. Saad, A. Bonen, K. C. Smith, and B. Benhabib, "Distributed-Force Recovery for a Planar Photoelastic Tactile Sensor," *IEEE International Conference on Instrumentation and Measurements*, Waltham, Massachusetts, 1995, pp. 532-537.

[3] R. E. Saad, A. Bonen, K. C. Smith, and B. Benhabib "Phase-lead Reconstruction of a Photoelastic Sensor," SPIE Vol. 2570, 1995. (In print).

[4] A. Cameron, R. Daniel and H. Durrant-Whyte, "Tactile Geometry for Images and Normal," in *Tactile Sensing and the Photoelastic Tactile Sensor,* Tech. Rep. OUEL 1758/89, Department of Engineering Science, University of Oxford, Oxford, 1989, pp. 1-16.

[5] K. W. Loh, H. Durrant-Whyte and R. Daniel, "A Photoelastic Tactile Sensor" Tech,. Rep. OUEL 1792/89. Department of Engineering Science, University of Oxford, Oxford, 1989.

[6] A. Cameron, R. Daniel and H. Durrant-Whyte, "Touch and Motion," *IEEE, International Conference on Robotics and Automation*, Philadelphia, 1988, pp. 1062-1067.

[7] L. D. Harmon, "Automated Tactile Sensing," International Journal of Robotics Research, Vol. 1, No. 2, 1982, pp. 3-32.

[8] F. Eghtedari and C. Morgan, "A Novel Tactile Sensor for Robot Applications", *Robotica*, Vol. 7, 1989, pp. 289-295.

[9] S. H. Hopkins, F. Eghtedari and D. T. Pham, "Algorithms for Processing Data from a Photoelastic Slip Sensor," *Mechatronics*, Vol. 2, No. 1, 1992, pp. 15-28.

[10] P. S. Theocaris and E. E. Gdoutos, *Matrix Theory of Photoelasticity*, Springer-Verlag, Berlin, 1979.

[11] K. Iizuka, *Engineering Optics*, Springer-Verlag, 2nd Ed., Germany, 1987.

[12] M. Shimojo, "Spatial Filtering Characteristic of Elastic Cover for Tactile Sensor," *IEEE International Conference on Robotics and Automation,* San Diego, CA, 1994, pp. 287-292.

[13] R. E. Ellis and M. Qin, "Singular-Value and Finite-Element Analysis of Tactile Shape Recognition," *IEEE International Conference on Robotics and Automation,* San Diego, CA, 1994, pp. 2529-2535.

[14] S. L. Ricker and R. E. Ellis, "2-D Finite-Element Models of Tactile Sensors," *IEEE International Conference on Robotics and Automation,* Atlanta, GA, 1993, pp. 941-947.

[15] F. Eghtedari, S. H. Hopkins, and D. T. Pham, "Model of a Slip Sensor," Journal of Engineering Manufacture, Vol. 207, 1993, pp. 55-64.

[16] A. Caiti, G. Canepa, D. De Rossi, F. Germagnoli, G. Magenes, and T. Parisini, "Towards the Realization of an Artificial Tactile System: Fine-Form Discrimination by a Tensorial Tactile Sensor Array and Neural Inversion Algorithms," IEEE Transactions on Systems, Man and Cybernetics, Vol. 25, No. 6, 1995, pp. 933-946.

[17] R. S. Fearing, "Planar Elasticity for Tactile Sensing," in *Advanced* Tactile *Sensing for Robotics*, Ed. H.R. Nicholls, World Scientific Publishing Co. Pte. Ltd., Singapore, 1992.